



**HAL**  
open science

## Near-Threshold and Resonance Effects in Rotationally Inelastic Scattering of D2O with Normal-H2

Astrid Bergeat, Alexandre Faure, Laurent Wiesenfeld, Chloé Miossec,  
Sébastien B. Morales, Christian Naulin

► **To cite this version:**

Astrid Bergeat, Alexandre Faure, Laurent Wiesenfeld, Chloé Miossec, Sébastien B. Morales, et al..  
Near-Threshold and Resonance Effects in Rotationally Inelastic Scattering of D2O with Normal-H2.  
Molecules, 2022, 27 (21), pp.7535. 10.3390/molecules27217535 . hal-03875820

**HAL Id: hal-03875820**

**<https://hal.science/hal-03875820>**

Submitted on 17 May 2024

**HAL** is a multi-disciplinary open access archive for the deposit and dissemination of scientific research documents, whether they are published or not. The documents may come from teaching and research institutions in France or abroad, or from public or private research centers.



L'archive ouverte pluridisciplinaire **HAL**, est destinée au dépôt et à la diffusion de documents scientifiques de niveau recherche, publiés ou non, émanant des établissements d'enseignement et de recherche français ou étrangers, des laboratoires publics ou privés.



Distributed under a Creative Commons Attribution 4.0 International License

## Article

# Near-Threshold and Resonance Effects in Rotationally Inelastic Scattering of D<sub>2</sub>O with *Normal*-H<sub>2</sub>

Astrid Bergeat <sup>1,\*</sup>, Alexandre Faure <sup>2</sup>, Laurent Wiesenfeld <sup>3</sup>, Chloé Miossec <sup>1</sup>, Sébastien B. Morales <sup>1</sup> and Christian Naulin <sup>1</sup>

<sup>1</sup> Univ. Bordeaux, CNRS, Bordeaux INP, ISM, UMR 5255, F-33400 Talence, France

<sup>2</sup> Univ. Grenoble Alpes, CNRS, IPAG, F-38000 Grenoble, France

<sup>3</sup> Laboratoire Aimé-Cotton, CNRS, Université Paris-Saclay, Bât 505, F-91405 Orsay, France

\* Correspondence: astrid.bergeat@u-bordeaux.fr

**Abstract:** We present a combined experimental and theoretical study on the rotationally inelastic scattering of heavy water, D<sub>2</sub>O, with *normal*-H<sub>2</sub>. Crossed-molecular beam measurements are performed in the collision energy range between 10 and 100 cm<sup>-1</sup>, corresponding to the near-threshold regime in which scattering resonances are most pronounced. State-to-state excitation cross-sections are obtained by probing three low-lying rotational levels of D<sub>2</sub>O using the REMPI technique. These measurements are complemented by quantum close-coupling scattering calculations based on a high-accuracy D<sub>2</sub>O–H<sub>2</sub> interaction potential. The agreement between experiment and theory is within the experimental error bars at 95% confidence intervals, leading to a relative difference of less than 7%: the near-threshold rise and the overall shape of the cross-sections, including small undulations due to resonances, are nicely reproduced by the calculations. Isotopic effects (D<sub>2</sub>O versus H<sub>2</sub>O) are also discussed by comparing the shape and magnitude of the respective cross-sections.



**Citation:** Bergeat, A.; Faure, A.; Wiesenfeld, L.; Miossec, C.; Morales, S.B.; Naulin, C. Near-Threshold and Resonance Effects in Rotationally Inelastic Scattering of D<sub>2</sub>O with *Normal*-H<sub>2</sub>. *Molecules* **2022**, *27*, 7535. <https://doi.org/10.3390/molecules27217535>

Academic Editor: Niels Engholm Henriksen

Received: 21 September 2022

Accepted: 29 October 2022

Published: 3 November 2022

**Publisher's Note:** MDPI stays neutral with regard to jurisdictional claims in published maps and institutional affiliations.



**Copyright:** © 2022 by the authors. Licensee MDPI, Basel, Switzerland. This article is an open access article distributed under the terms and conditions of the Creative Commons Attribution (CC BY) license (<https://creativecommons.org/licenses/by/4.0/>).

**Keywords:** inelastic collisions; cross-sections; water; hydrogen

## 1. Introduction

Water is the third most abundant molecule in the interstellar medium (ISM) and has ubiquitously been observed by ground- and space-based telescopes since its first detection in 1969 in the Orion nebula [1,2]. Water thus is a key molecule for understanding the energy balance and the physical–chemical processes that occur in these environments. Despite the low elemental deuterium abundance in the Galaxy,  $D/H \sim 10^{-5}$ , a spectacular deuterium enrichment of various interstellar molecules, has been observed in star forming regions. Among these molecules, the deuterated water isotopologues HDO and D<sub>2</sub>O are of special importance because they can help to understand the origin of water in protostars [3].

D<sub>2</sub>O was identified for the first time in 2007 toward IRAS 16293-2422 [4] in its *para* form and detected in its *ortho* form in 2010 in the same cold and diluted protostar envelope [5], which has then allowed to derive the *ortho*-to-*para* ratio of D<sub>2</sub>O (< 2.6. For comparison, the thermal equilibrium value is 2).

However, in order to interpret the astrophysical observations [2] in terms of relative abundances or even local physical conditions, radiative transfer modeling is necessary, as the molecular populations are generally far from local thermodynamical equilibrium. At low density, the heavy water population is indeed determined by a competition between the radiative and collisional processes, thus requiring the knowledge of rates for collisional (de)excitation. Its principal collision partner obviously is H<sub>2</sub> because of its high abundance in the cold ISM.

Inelastic collisions between molecules are fundamental processes in which energy is transferred between their relative translational motion and their internal degrees of freedom. Water–hydrogen collisions play an essential role in a large variety of properties

or research fields (thermal conductivity, transport properties for water diluted in molecular hydrogen, or the dynamics of molecular hydrogen confined in the cages of clathrate hydrates) and allow to better understand the non-covalent interactions between molecules of great importance for energy applications, combustion chemistry, and astrochemistry. The efficiency of the inelastic process (i.e., whether a collision does or does not promote the molecule in a given state into another state) is governed by the state-to-state integral cross-section (ICS,  $\sigma$ ), which is a function of molecular energy state, colliding partner, and relative translational energies. Excitation requires that the collision energy of the impact be sufficient to reach the upper state, which at sufficiently low temperature becomes energetically impossible. It should be noticed that the rate coefficients are calculated by averaging the product  $\sigma \times v_r$  over a thermal distribution of relative velocities  $v_r$ .

If inelastic scattering ICS is zero below the threshold energy (the energy needed to promote the molecule from its initial state to an upper final state), above this threshold, classical mechanics predicts that it rises sharply to a maximum and then decreases smoothly at higher energies [6]. However, quantum mechanics show that at low kinetic energies, the inelastic scattering ICS of simple molecular species colliding with  $H_2$  do not follow such a simple threshold law but are instead highly structured, particularly in the vicinity of the thresholds of the lowest molecular rotational excitations. Such behavior of the ICS characterizes the interaction potential between the colliding partners and is very sensitive to the shape of this potential energy surface (PES).

The rotational energy levels of  $D_2O$  are labelled by the quantum number  $j_{D_2O}$  and the two pseudo-quantum numbers  $k_a$  and  $k_c$ , which are the projections of  $j_{D_2O}$  along the principal inertia axis,  $a$ - and  $c$ -axes, respectively. The  $C_2$  symmetry axis corresponds to the  $b$ -axis, the  $a$ -axis being in-plane and perpendicular to the  $b$ -axis. The rotation around the  $c$ -axis is in the molecular plane. For a given  $j_{D_2O}$ ,  $k_a = j_{D_2O}$  and  $k_c = j_{D_2O}$  correspond to rotation around the  $a$ - and  $c$ -axes, respectively. *Para*- and *ortho*- $D_2O$  levels are characterized by  $k_a + k_c$  odd and even, respectively, in accordance with the symmetry relations for bosons, due to the nuclear spin of D atoms. As no atom exchange is possible at the studied collision energies and as the *ortho* and *para* levels do not interconvert in inelastic collisions, these are presented separately in Figure 1. The rotational levels of  $H_2$  are labelled by the angular momentum  $j_{H_2}$ , with  $j_{H_2}$  even for *para*- $H_2$  and  $j_{H_2}$  odd for *ortho*- $H_2$  due to the fermionic nuclei.

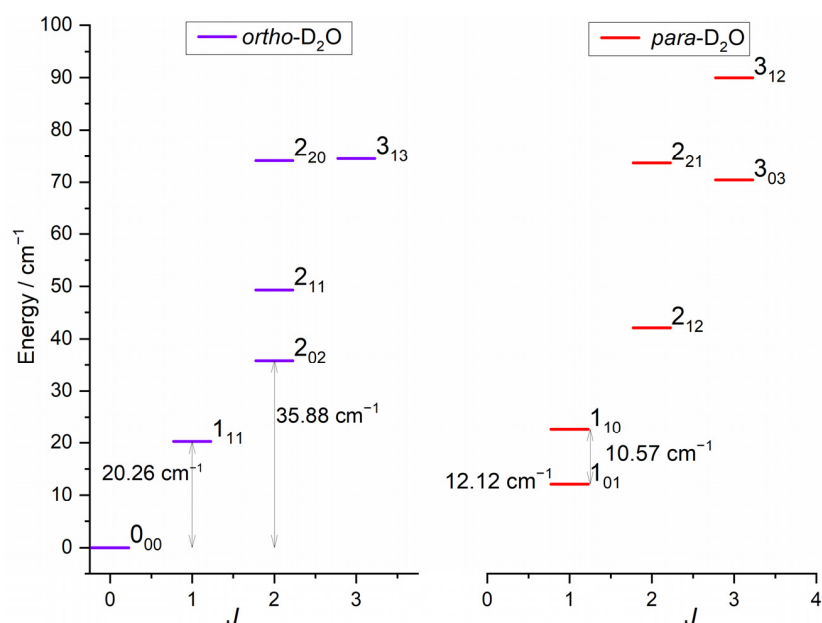


**Figure 1.** Rotational energy levels of the water isotopologue,  $D_2O$ , for  $E < 100 \text{ cm}^{-1}$  [7]. Levels are labelled by  $j_{k_a k_c}$ . Ortho levels ( $D_2O$ ,  $k_a + k_c$  even) are depicted in left panel and para levels in right panel.

Previous theoretical studies of the H<sub>2</sub>O–H<sub>2</sub> interactions are too extensive to be enumerated in detail herein. The reader may refer to the last articles on rotational inelastic collisions and citations herein [8,9] and, therefore, we will limit our review to only a portion of the literature pertinent to our experiments, mainly the various experimental results on H<sub>2</sub>O–H<sub>2</sub> and the theoretical calculations and experiments on D<sub>2</sub>O–H<sub>2</sub>.

In the first molecular beam scattering experiment on H<sub>2</sub>O + H<sub>2</sub> elastic differential cross-sections [10], well resolved diffractive oscillations were observed, as well as the rainbow maximum. The spherically symmetric model potential parameters (e.g., the well depth and location of zero potential) were deduced assuming a Lennard–Jones (12,6) potential. The H<sub>2</sub>–H<sub>2</sub>O van der Waals complex was then studied by infrared spectroscopy in the gas phase by the group of D. Nesbitt [11,12] and also in matrix [13]. There are also studies on H<sub>2</sub>O pressure broadening by H<sub>2</sub> [14,15] or inelastic collisions [16,17]. The Perugia group has reported determination of the potential parameters for the isotropic component of the D<sub>2</sub>O–D<sub>2</sub> interaction by elastic scattering studies [18]. The group of Nesbitt and coworkers has also studied the infrared spectrum of the H<sub>2</sub>O–D<sub>2</sub> complex in the bend mode frequency region [19].

A large number of studies can thus be found in the literature providing information on H<sub>2</sub>O–H<sub>2</sub>, whereas calculations or experiments on D<sub>2</sub>O–H<sub>2</sub> are scarce. The complex has been studied in solid neon matrix [13] where the infrared absorptions principally arose from complexes involving *ortho*-H<sub>2</sub>, for which  $j_{H_2} = 1$ . Excitation rate constants of the D<sub>2</sub>O low lying rotational transitions by *para*-H<sub>2</sub> were calculated for temperatures between 1 and 30 K [20] and later completed for temperatures below 100 K [21]. The calculations at the close-coupling level were performed using the highly accurate full 9D (but vibrationally averaged to 5D) PES of Valiron et al. [22]. In the cold or near cold regime (5–30 K, relevant for astrophysical applications), prominent open channel (orbiting) and closed channel (Feshbach) resonances were observed. The first state-to-state differential cross-sections (DCSs) for rotationally inelastic scattering of D<sub>2</sub>O(0<sub>00</sub> or 1<sub>01</sub>) + H<sub>2</sub>( $j_{H_2} = 0, 2$  or 1) were measured by Sarma et al. [23] at the collision energy of 584 cm<sup>−1</sup>. At collision energies above 500 cm<sup>−1</sup>, this crossed-beam study could only probe the PES in the short-range and well regions. The first experimental check at long range was achieved by measuring the state-to-state scattering ICSs of rotationally inelastic excitation of D<sub>2</sub>O in the 2<sub>02</sub> level by collisions with *para*-H<sub>2</sub> [8], in the very low collision energy range 10–100 cm<sup>1</sup> (near rotational thresholds). The observed scattering resonances were unambiguously identified by quantum mechanical calculations performed on the PES of Valiron et al. [22]. The aim of this study is (i) to present the full set of experimental ICSs for the D<sub>2</sub>O low lying rotational transitions colliding with *normal*-H<sub>2</sub> in the vicinity of the thresholds and (ii) to provide new stringent tests of theory as the experimental ICS resonance structures (amplitude and position) are very sensitive to the shape and even to tiny details of the PES.

In the results section, our beam characteristics and the experimentally measured crossed beam ICSs will be presented followed by the main theoretical results in relation with our experimental studies. The experimental observations will be compared with the inelastic scattering calculations in the discussion section.

## 2. Results

### 2.1. Experimental Results

The experimental results were obtained in a crossed-molecular beam (CMB) experiment under single collision conditions (see Figure 2). Our machine allows inelastic processes [24] to be studied at low collision energies. For this purpose, two supersonic molecular beams, one composed of deuterated water seeded in a carrier gas and the other of pure hydrogen, are generated with a high velocity resolution, while most of the initial population of molecular species being in their ground rotational state. The collision energy of the colliding partners is tuned by varying the beam intersection angle,  $\gamma$ :

$$E_{\text{collision}} = \frac{1}{2}\mu v_r^2 = \frac{1}{2}\mu(v_{D_2O}^2 + v_{H_2}^2 - 2v_{D_2O}v_{H_2}\cos\gamma) \quad (1)$$

where  $v_{D_2O}$  and  $v_{H_2}$  are the velocities of the  $D_2O$  and  $H_2$  beams,  $\mu$  is the reduced mass of the system  $D_2O-H_2$ , and  $v_r$  is their relative velocity. The state-to-state ICS is measured by resonance-enhanced multiphoton ionization (REMPI) coupled with time-of-flight mass spectrometry (TOF-MS), using tunable UV/VUV lasers (see the Methods section for more details). We describe the characteristics of each beam, which has an impact on the experimental results before presenting the experimental ICSs.

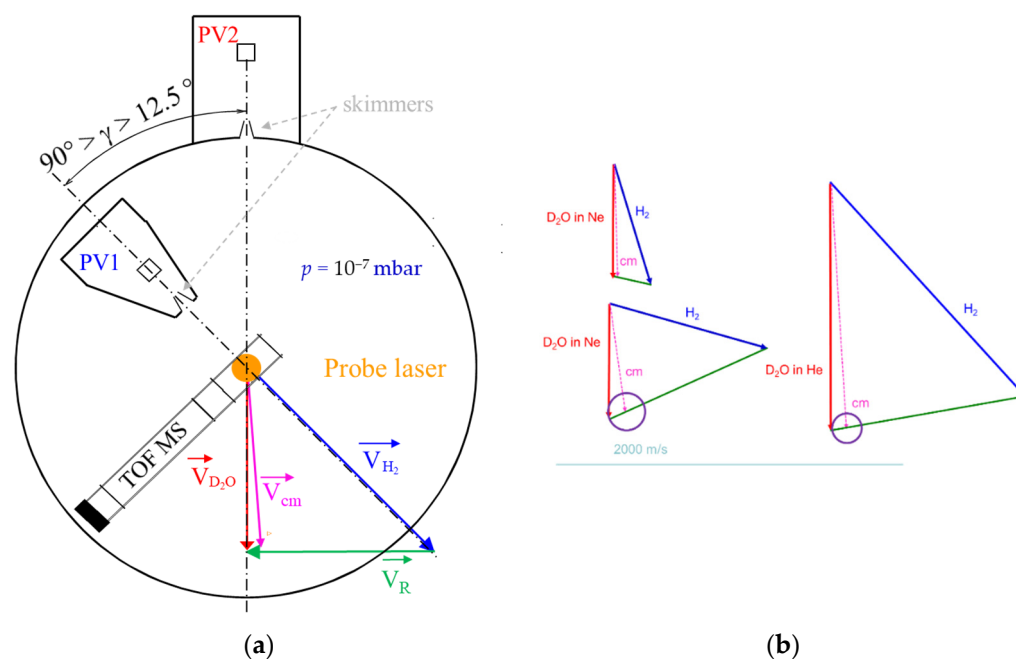


**Figure 2.** (a) The crossed molecular beam apparatus with variable angle,  $\gamma$  from  $12.5^\circ$  to  $90^\circ$ ; between the two beam axes generated by pulsed valves (PV); (b) Newton diagrams for  $D_2O$  seeded in Ne collisions with *normal*- $H_2$  at  $13^\circ$  and  $70^\circ$  and for  $D_2O$  seeded in He collisions with *normal*- $H_2$  at  $35^\circ$ . The radii of the circles represent the velocities of rotationally excited  $D_2O$  in the center-of-mass (c.m.) frame and the green vector, the relative velocities of the colliders.

The  $D_2O$  or *normal*- $H_2$  beams are generated using Even–Lavie valves. The measured characteristics of the gas pulses, velocity, pulse duration, velocity spread, and angle spread (see Section 4) are reported in Table 1.

**Table 1.** Characteristics of the molecular beams used in the determination of the integral cross-sections.

Beam	Velocity <sup>1</sup> /m s <sup>-1</sup>	Velocity Spread <sup>1</sup> HWHM/m s <sup>-1</sup>	Pulse Duration <sup>2</sup> HWHM/ $\mu$ s	Angle Spread <sup>3</sup> HWHM/ $^\circ$
$D_2O$ in He	$1858 \pm 30$	44	15.0	0.79
<i>normal</i> - $H_2$ at 145 K	$1959 \pm 30$	44	7.9	1.17
$D_2O$ in Ne	$853 \pm 24$	14	19.3	0.71
<i>normal</i> - $H_2$ at 10 K	$947 \pm 28$	49	11.5	1.17

<sup>1</sup> Beam velocity peak values and half width at half maximum (HWHM) of the velocity spread deduced from temporal profiles at the crossing point and 393.3 mm downstream. <sup>2</sup> Pulse duration (HWHM) at the crossing point. <sup>3</sup> Angular divergence (HWHM).

### 2.1.1. $D_2O$ Beam

Two carrier gases were used for the  $D_2O$  beam, namely He and Ne, leading to beams with different characteristics (see Table 1). From the REMPI spectra reported in Figure 3, the  $D_2O$  rotational distribution was determined using the spectroscopic data of the  $C^1B_1$ ,  $v' = 0 \leftarrow X^1A_1$ ,  $v = 0$  transitions, from Yang et al. [25] provided in PGopher software [26]. In our previous study on  $D_2O + para$ - $H_2$  [8], a rotational temperature of 12 K was determined for the  $D_2O$  beam seeded in He, with a spin temperature of 320 K, corresponding to the reservoir temperature. The rotational populations were thus 0.55, 0.19, 0.15, 0.05, and

0.04, for the  $0_{00}$ ,  $1_{01}$ ,  $1_{11}$ ,  $1_{10}$ , and  $2_{02}$  levels, respectively. Further investigation of the contributions of the different rotational levels on the ICSs for the transitions to the  $D_2O$   $2_{02}$  rotational level allowed us to refine the rotational population ratio of  $D_2O$  ( $0_{00}$ : $1_{11}$ ) and ( $1_{01}$ : $1_{10}$ ) to 0.81:0.19 and 0.73:0.27, respectively. New experimental inelastic collision studies were performed with this beam of  $D_2O$  diluted in He and supplemented with  $D_2O$  seeded in Ne. For the latter beam, the REMPI spectrum is given in Figure 3. Obviously, only the lowest rotational levels of *ortho*- $D_2O$  and *para*- $D_2O$  are populated: the inset is the enlargement of the spectrum range where the first excited rotational levels may be seen and were estimated to have a population of less than 2%. As these signals are almost within the noise (see the inset of the  $D_2O$  spectrum) even if the transitions are favored for the excited states, only the ground rotational levels will significantly contribute to the inelastic collisions.

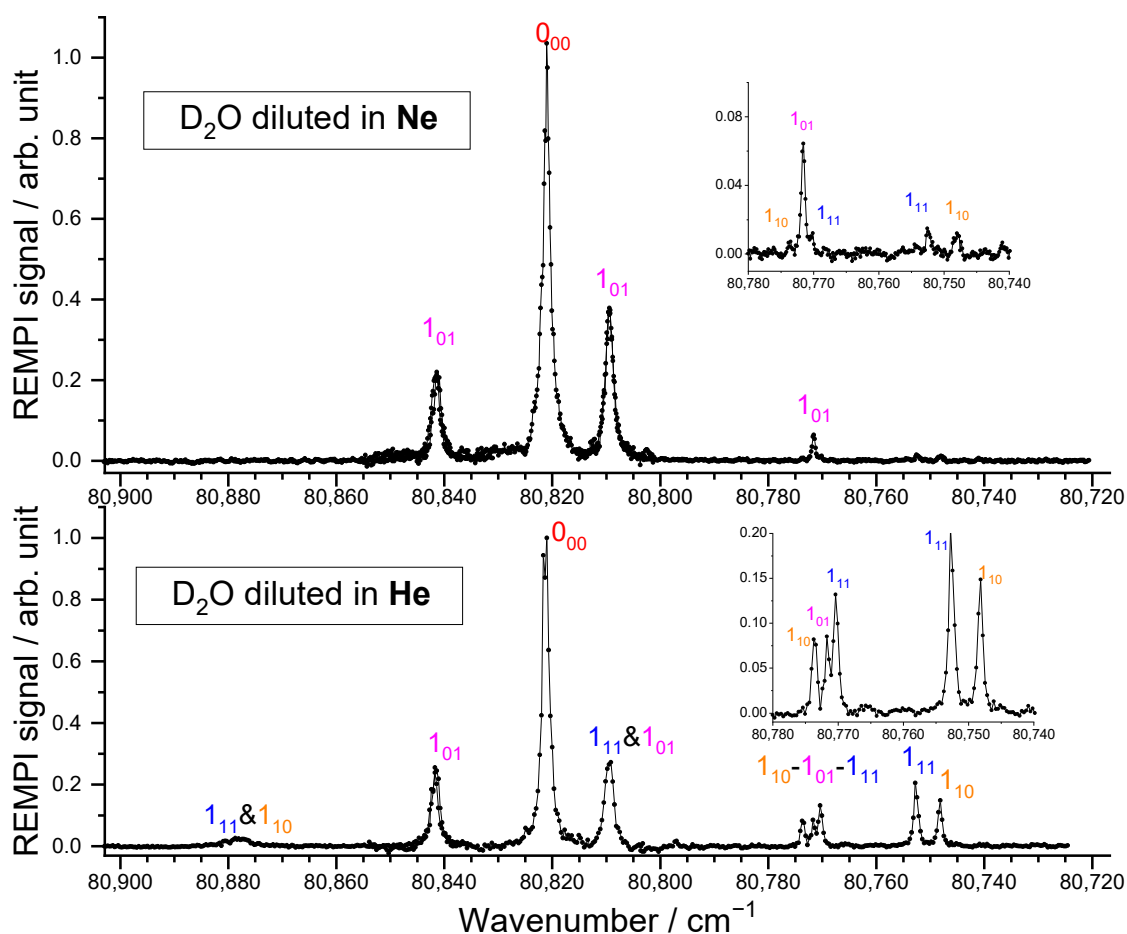


**Figure 3.** A  $(2 + 1)$  REMPI spectrum of the  $C^1B_1, v' = 0 \leftarrow X^1A_1, v = 0$  transition of  $D_2O$  in the supersonic beam when Ne (top) or He (bottom) is used as a carrier gas. The inset is the enlargement of a part of the spectrum. The labels indicate the rotational levels,  $j_{k_a k_c}$ , from which the transitions originate. See Yang et al. [25] for more details.

Indeed, rotational cooling is more efficient when water molecules are seeded in Ne rather than in He [25]. However, even if the cooling is rapid, hence avoiding condensation, dimers may be formed, i.e., a weakly bound van der Waals structure, which presents shallow minima of  $\sim 34$  and  $7 \text{ cm}^{-1}$  for  $D_2O$ -Ne [27] and  $D_2O$ -He clusters [28], respectively. Usually, a large cluster binding energy enhances the formation of clusters, which release their condensation energy into the beam, thence limiting translational cooling. However, the characteristics of the beams are equivalent with or without  $D_2O$ . Moreover, no signal at higher  $m/z$  than those of  $D_2O^+$  was detected. In conclusion, there is no evidence of significant amounts of water clusters in the beam.



As carrier gas mass changes, the beam velocity changes, too (see Table 1). The terminal velocity  $v$  of a supersonic beam generated by an adiabatic and isentropic expansion of an ideal gas through a nozzle, from a reservoir at a temperature  $T_0$ , is defined by:

$$\frac{1}{2}mv^2 = \int_T^{T_0} C_p dT, \quad (2)$$

where the temperature of the beam is  $T \ll T_0$  (substantial cooling in the expansion), and  $C_p$  is the average molar heat capacity (for an atom,  $C_p = 5/2 R$ , where  $R$  stands for the perfect gas constant). This equation implies a velocity ratio of  $\sqrt{(20/4)} = 2.2$  for the two carrier gas, which is experimentally observed (see Table 1, where  $1858/853 = 2.2$ ).

### 2.1.2. Normal-H<sub>2</sub> Beam

As the best collisional energy resolution is obtained when the two beams have almost the same velocity (Figure 2), for the H<sub>2</sub> beam, a cryogenically cooled valve was used with He closed-cycle cryostats (Equation (2)). The temperature of the cold head was reduced at its minimum, which corresponds to a setpoint of 10 K to reach the lowest hydrogen beam velocity, which is almost equal to the neon beam velocity (Table 1). In the case of water diluted in He, a setpoint at 145 K was used. However, even if the temperature in the reservoir is decreased to a setpoint of 145 K or 10 K, there is no *ortho-to-para* conversion of the hydrogen. *Normal-H<sub>2</sub>* beam remains a mixture of *para*- and *ortho*-H<sub>2</sub> with the room temperature ratio, i.e., 3:1. The H<sub>2</sub> beam was probed (Figure 4) when recording ( $C^1\Pi_u; v = 2 \leftarrow X^1\Sigma_g^+; v = 0$ ) R(0) and R(1) transitions near 96.47 nm, with a (3 + 1) REMPI scheme at 289.4 nm [29]. No evidence of R(2) signal was found for the beam with the highest reservoir temperature: a *normal-H<sub>2</sub>* beam is composed of 25% of H<sub>2</sub>( $j_{H_2} = 0$ ) and 75% of H<sub>2</sub>( $j_{H_2} = 1$ ).

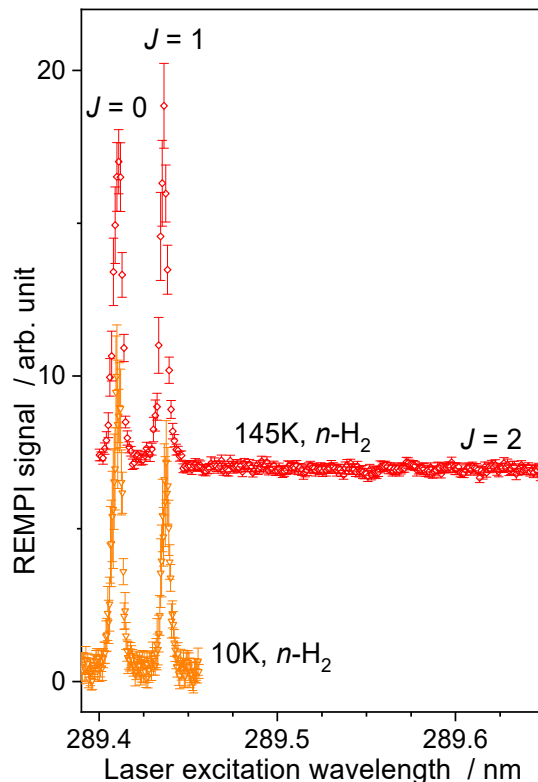


**Figure 4.** The (3 + 1) REMPI spectra [29] of normal-H<sub>2</sub> beams. Temperature (145 K or 10 K) is the set point of the cold head. Vertical error bars correspond to statistical uncertainties at 95% of the confidence interval.

### 2.1.3. Integral Cross-Sections

Three rotational levels of D<sub>2</sub>O were probed: 1<sub>11</sub>, 2<sub>02</sub> for *ortho*-D<sub>2</sub>O, and 1<sub>10</sub> for *para*-D<sub>2</sub>O. The REMPI intensities were recorded versus the angle relative to the beam axes. Collision energies were derived from Equation (1). The cross-section was obtained from the REMPI signal intensity, divided by the relative velocity of D<sub>2</sub>O and H<sub>2</sub> and the interaction time of the two beams (see the Methods section for more details).

The beam characteristics are given in Table 1. In Figure 5, whatever the seeded gas was for the water beam and thus the temperature of the hydrogen beam, the cross-sections are well reproduced: the thresholds are at the correct energies (20.3 and 10.6 cm<sup>-1</sup> for the 0<sub>00</sub>–1<sub>11</sub> and 1<sub>01</sub>–1<sub>10</sub> excitation, respectively), and we can observe some resonances at the same energies. There is thus no evidence of any clusters in the beams, as the binding energies of He–D<sub>2</sub>O and Ne–D<sub>2</sub>O differ by 30 cm<sup>-1</sup>, and the D<sub>2</sub>O + H<sub>2</sub> resonances are observed at the same collision energies for the two water carrier gases. However, compared to the ICSs measured when D<sub>2</sub>O is seeded in Ne, they are broadened and slightly less marked in the case of D<sub>2</sub>O seeded in He. In fact, the collision energy spread is larger (Figure 6), resulting in a spread-out of the resonance features over a more extended collision energy range. Moreover, the signal starts from a negative value in Figure 5a: the 1<sub>11</sub> rotational population starts decreasing when H<sub>2</sub> collides with D<sub>2</sub>O. Indeed, in the D<sub>2</sub>O:He beam, the first two rotational levels of *ortho*-D<sub>2</sub>O and *para*-D<sub>2</sub>O are populated, leading to the de-excitation of the 1<sub>11</sub> excited state until the collision energy is large enough to promote the excitation from the ground state (0<sub>00</sub> → 1<sub>11</sub>). When the 1<sub>10</sub> excited rotational level is probed (Figure 5b), the lowest collision energy, which corresponds to our lowest angle between the two beams, is above the threshold (1<sub>01</sub> → 1<sub>10</sub>), not allowing the observation of the de-excitation. In the case of D<sub>2</sub>O:Ne, only the ground rotational levels are populated (see Figure 3). Thus, in Figure 5, there is only one contribution from the ground rotational level to the probed excited one: the 0<sub>00</sub> → 1<sub>11</sub> and 1<sub>01</sub> → 1<sub>10</sub> transitions in Figure 5a,b, respectively.

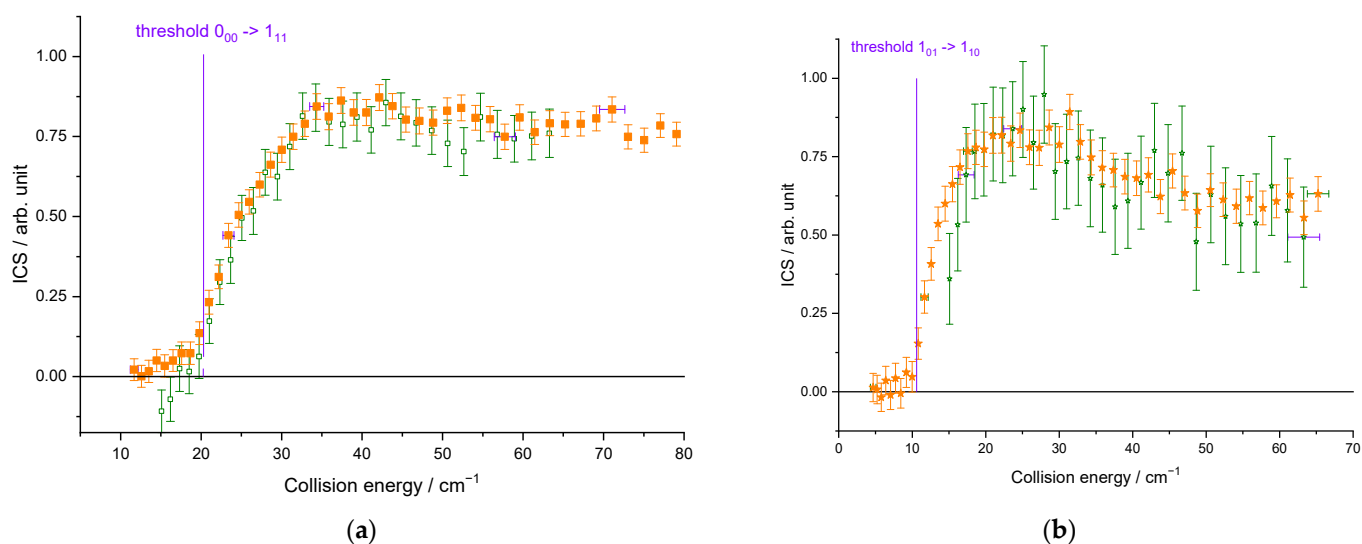


**Figure 5.** Experimental cross-sections for different conditions: in orange and in green, for D<sub>2</sub>O seeded in Ne and in He, respectively: (a) for the D<sub>2</sub>O(0<sub>00</sub>) → D<sub>2</sub>O(1<sub>11</sub>) transition; (b) for the D<sub>2</sub>O(1<sub>01</sub>) → D<sub>2</sub>O(1<sub>10</sub>) transition. Negative values for the cross-sections mean that the rotational population probed decreases: loss of the population on the 1<sub>10</sub> level by transition to the 1<sub>01</sub> or 2<sub>12</sub> levels and loss of the 1<sub>11</sub> population by transition to the 0<sub>00</sub> or 2<sub>02</sub> levels. Vertical error bars correspond to statistical uncertainties at 95% of the confidence interval.



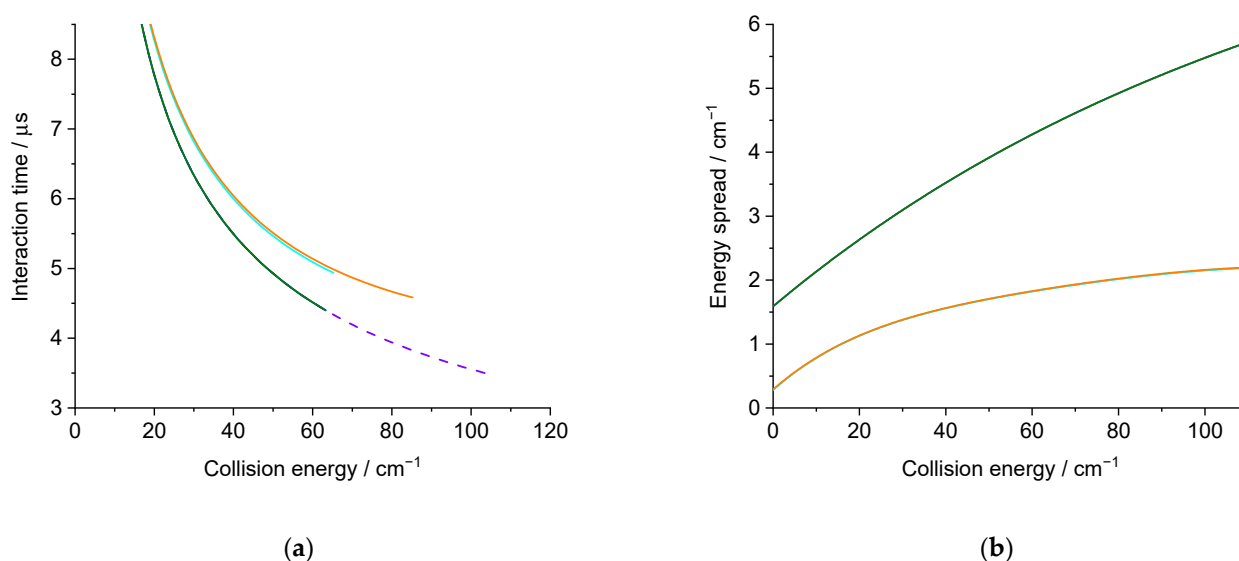


**Figure 6.** (a) Interaction time for an isotropic distribution; (b) collision energy spread calculated for the experimental conditions: in orange (green) solid lines,  $\text{D}_2\text{O}$  seeded in  $\text{Ne}(\text{He})$  for the  $\text{D}_2\text{O}(0_{00}) \rightarrow \text{D}_2\text{O}(1_{11})$  or  $\text{D}_2\text{O}(1_{01}) \rightarrow \text{D}_2\text{O}(1_{10})$  transition, and in purple dashed line,  $\text{D}_2\text{O}$  seeded in  $\text{He}$  for the  $\text{D}_2\text{O}(0_{00}) \rightarrow \text{D}_2\text{O}(2_{02})$  transition.

Each experimental ICS datum corresponds to an average over a Gaussian distribution of collision energies: the half width at  $1/e$  height, called collision energy spread, is given in Figure 6b. More details are given in the Methods section. This collision energy spread originates from the velocities and angular spread (Table 1). It will also affect the average relative velocity and the interaction time, which is given in Figure 6a. As the deconvolution of the experimental points is not possible, the theoretical cross-sections are convoluted with the collision energy spread to allow for comparison with the experimental data. Moreover, as previously explained, the rotational population distribution is also taken into account.

## 2.2. Theoretical Results

Inelastic scattering calculations were performed in a similar way to Bergeat et al. [8], and a summary can be found in the Methods section. The theoretical cross-sections for three particular rotational excitations from the *ortho*- $\text{D}_2\text{O}$  ground state by collisions with  $\text{H}_2$  are plotted in Figures 2 and 3.

Calculations were performed for  $\text{H}_2$  in its ground *para* ( $j_{\text{H}_2} = 0$ ) and *ortho* ( $j_{\text{H}_2} = 1$ ) states, and cross-sections for *normal*- $\text{H}_2$  were obtained for an *ortho*-to-*para* ratio fixed at 3. The rotational basis set for  $\text{D}_2\text{O}$  included angular momenta up to  $j_{\text{D}_2\text{O}} = 6$ , corresponding to the lowest 25 *para*- and lowest 25 *ortho*- $\text{D}_2\text{O}$  levels. The lowest two levels were included in the basis set for *para*- $\text{H}_2$  ( $j_{\text{H}_2} = 0, 2$ ) and *ortho*- $\text{H}_2$  ( $j_{\text{H}_2} = 1, 3$ ). Enlarging the  $\text{D}_2\text{O}$  or  $\text{H}_2$  basis sets was found to be negligible at the investigated energies, with cross-sections changing by less than one percent. We note, however, that because of the potential well ( $D_e = 238 \text{ cm}^{-1}$ ) and anisotropy of the  $\text{D}_2\text{O}-\text{H}_2$  PES, the inclusion of closed-channels was found to be crucial, even for *ortho*- $\text{H}_2$ .

As previously noted for the  $\text{H}_2\text{O}-\text{H}_2$  system [17] and also for other molecule- $\text{H}_2$  systems [30], resonances are more conspicuous for *para*- $\text{H}_2$  ( $j_{\text{H}_2} = 0$ ) than for *ortho*- $\text{H}_2$  ( $j_{\text{H}_2} = 1$ ). This is particularly striking here for the  $0_{00} \rightarrow 2_{02}$  transition (Figure 7) where resonances have magnitudes up to twice that of the background cross-section for *para*- $\text{H}_2$  ( $j_{\text{H}_2} = 0$ ) while for *ortho*- $\text{H}_2$  ( $j_{\text{H}_2} = 1$ ) are much less intense. This can be explained by the non-vanishing quadrupole of *ortho*- $\text{H}_2$  ( $j_{\text{H}_2} = 1$ ) and the corresponding stronger binding with *ortho*- $\text{H}_2$  ( $j_{\text{H}_2} = 1$ ) than with *para*- $\text{H}_2$  ( $j_{\text{H}_2} = 0$ ). This was observed in the  $\text{H}_2\text{O}-\text{H}_2$  complex where the dissociation energy and number of bound-states are indeed significantly larger for *ortho*- $\text{H}_2$  ( $j_{\text{H}_2} = 1$ ) monomers than *para*- $\text{H}_2$  ( $j_{\text{H}_2} = 0$ ) monomers [31]. Overlapping and

broadened resonances are thus expected to be more numerous in  $D_2O$ -*ortho*- $H_2$  ( $j_{H_2} = 1$ ) with respect to  $D_2O$ -*para*- $H_2$  ( $j_{H_2} = 0$ ). In addition, it is observed that the background cross-sections for *para*- $H_2$  ( $j_{H_2} = 0$ ) and *ortho*- $H_2$  ( $j_{H_2} = 1$ ) have similar magnitudes for the transition  $0_{00} \rightarrow 2_{02}$  while *ortho*- $H_2$  ( $j_{H_2} = 1$ ) cross-sections are much larger than *para*- $H_2$  ( $j_{H_2} = 0$ ) cross-sections for other transitions, e.g.,  $0_{00} \rightarrow 1_{11}$  and  $1_{11} \rightarrow 2_{02}$  (Figure 8). This is clearly due to the dipole–quadrupole interaction, which dominates in  $D_2O$  dipolar transitions (i.e., those with  $\Delta j_{D_2O} = 0, \pm 1$ ,  $\Delta k_a = \pm 1$ ,  $\Delta k_c = \pm 1$ ) while  $D_2O$  quadrupolar transitions ( $\Delta j_{D_2O} = \pm 2$ ) are much less sensitive to the quadrupole of  $H_2$ .

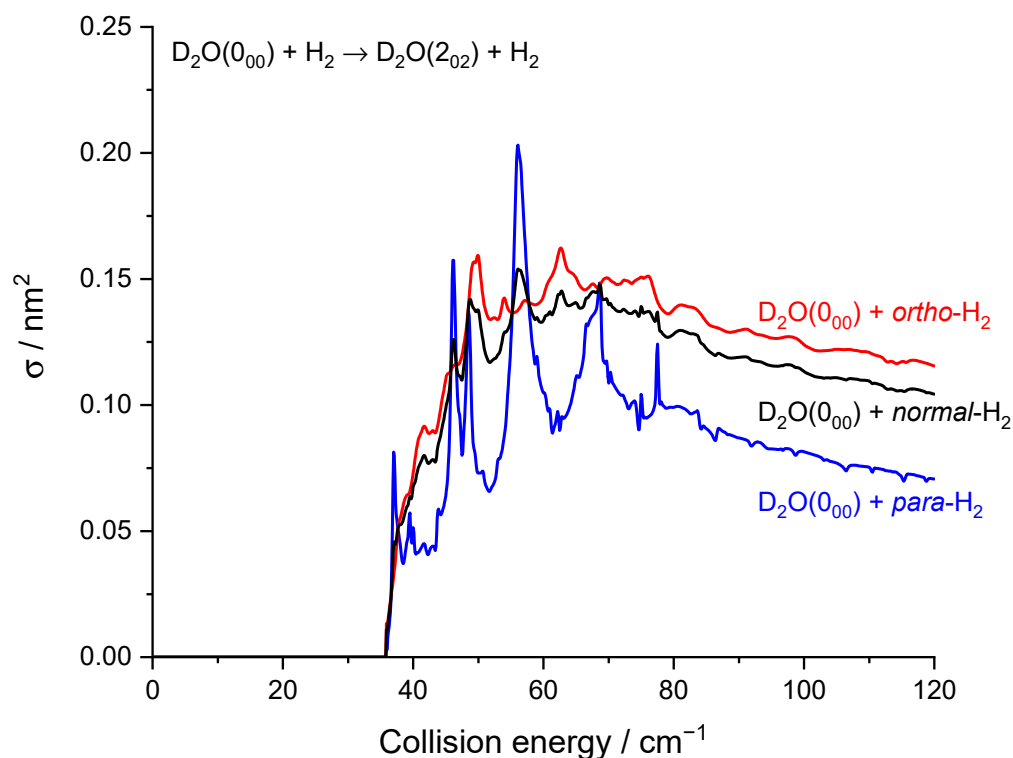


**Figure 7.** Rotational excitation cross-sections for the  $D_2O$   $0_{00}$ - $2_{02}$  transition in blue *para*- $H_2$  ( $j_{H_2} = 0$ ), in red *ortho*- $H_2$  ( $j_{H_2} = 1$ ), and in black *normal*- $H_2$  ( $j_{H_2} = 0$  and 1).

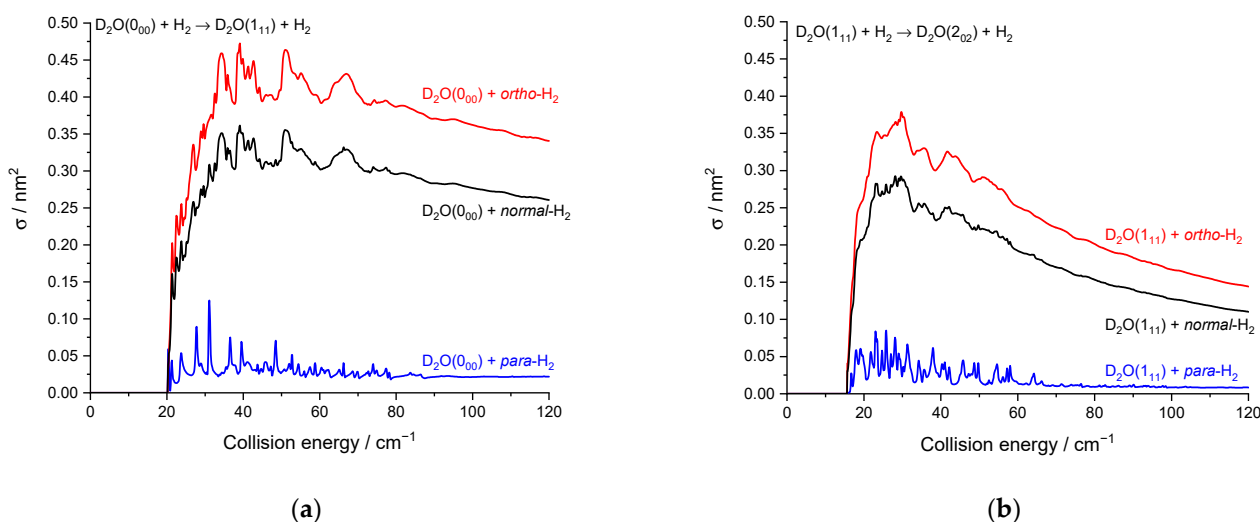


**Figure 8.** Rotational excitation cross-sections in blue  $D_2O$  + *para*- $H_2$  ( $j_{H_2} = 0$ ), in red  $D_2O$  + *ortho*- $H_2$  ( $j_{H_2} = 1$ ), and in black  $D_2O$  + *normal*- $H_2$  ( $j_{H_2} = 0$  and 1): (a) for the  $0_{00}$ - $1_{11}$  transition; (b) for the  $1_{11}$ - $2_{02}$  transition.

### 3. Discussion

To compare the experimental results with the theoretical cross-sections, the calculated ICSs were convoluted with the experimental collision energy spread, and the different contributions of the rotational populations were added or subtracted with the appropriated weights (Table 2), as explained in the Methods section. To begin, the *para* to *ortho* ratios were kept constant at their values at 320 K as the *ortho-para* conversion rates are extremely slow without any magnetic catalyst: 2:1 for D<sub>2</sub>O and 3:1 for H<sub>2</sub> (see Table 2). In Figure 9a, only one state-to-state contribution is observed, the D<sub>2</sub>O(1<sub>01</sub>) + *normal*-H<sub>2</sub> → D<sub>2</sub>O(1<sub>10</sub>) + *normal*-H<sub>2</sub>. This is because only the lowest *para*- and *ortho*-D<sub>2</sub>O rotational levels are significantly populated when seeded in Ne. The overall excitation function, i.e., the evolution of the ICS versus the collision energy, is in good agreement with the convoluted theoretical calculations. In the case of the excitation transition from D<sub>2</sub>O(0<sub>00</sub>) to D<sub>2</sub>O(1<sub>11</sub>) shown in Figure 10a, small undulations due to resonances are observed in perfect agreement with the quantum mechanical calculations. However, we should underline that a small contribution of 0.12 on the 1<sub>01</sub> to 2<sub>12</sub> transition was added to take into account the overlap of the REMPI peak from the probed 1<sub>11</sub> rotational level of D<sub>2</sub>O with those from the 2<sub>12</sub> level. Then, the REMPI intensities for the D<sub>2</sub>O(1<sub>10</sub>) were recorded when heavy water was seeded in He (Figure 9b). Due to higher beam velocities, the minimum collision energy probed is above threshold. Furthermore, the signal is small as some population in the excited state is lost by de-excitation to the ground state and excitation to the next upper state. No real structure was observed. The 1<sub>10</sub> to 1<sub>01</sub> population ratio of the water beam in He was deduced from this excitation function and used for the other fits, despite the uncertainty. The 1<sub>11</sub> to 0<sub>00</sub> population ratio was then fitted from the 2<sub>02</sub> experimental ICSs (Figure 11), using the overlap value of the REMPI peaks from 2<sub>12</sub> and 2<sub>02</sub> determined previously [8]. All these population ratios and REMPI peak overlaps summarized in Table 2 were also used to analyze the ICSs of the D<sub>2</sub>O(1<sub>11</sub>) transitions when water is seeded in He. The very good agreement between theory and experiment in Figure 10b, confirmed the accuracy of our experimental treatment and the theoretical calculations.

**Table 2.** Rotational population distributions in the D<sub>2</sub>O beam seeded in He or Ne and contribution to the main rotational level probed by another rotational level.

Contributions	D <sub>2</sub> O in He	D <sub>2</sub> O in Ne
<i>ortho</i> -D <sub>2</sub> O: <i>para</i> -D <sub>2</sub> O <sup>1</sup>	2/3:1/3	2/3:1/3
0 <sub>00</sub> :1 <sub>11</sub> <sup>2</sup>	90:10	100:0
1 <sub>01</sub> :1 <sub>10</sub> <sup>2</sup>	83:17	100:0
2 <sub>12</sub> in 2 <sub>02</sub> <sup>3</sup>	0.20	
2 <sub>12</sub> in 1 <sub>11</sub> <sup>3</sup>	0.12	0.12

<sup>1</sup> The *ortho*-to-*para* ratio of D<sub>2</sub>O remains at the room temperature equilibrium ratio of 2. <sup>2</sup> The relative population ratio of the two *ortho*- or *para*-D<sub>2</sub>O first rotational levels. <sup>3</sup> The relative contribution of the 2<sub>12</sub> rotational level to the signal of the 2<sub>02</sub> or 1<sub>11</sub> level due to an overlap of the lines in the REMPI spectra (see the text for details).

The resonances observed for the 0<sub>00</sub>-2<sub>02</sub> rotational inelastic cross-sections occur because of quasi-bound states become transiently accessible during the collision. They were characterized by analyzing partial cross-sections differing by their total angular momentum *J* [8]. The total cross-section (summed over all partial waves *J*) was found to show, on resonance, large contributions from specific orbital angular momentum *l*, the rotational states of H<sub>2</sub>, and D<sub>2</sub>O being *j*<sub>D<sub>2</sub>O</sub> = 0 and *j*<sub>H<sub>2</sub></sub> = 0. An analysis of the resonances was put forward in the preceding paper [8].

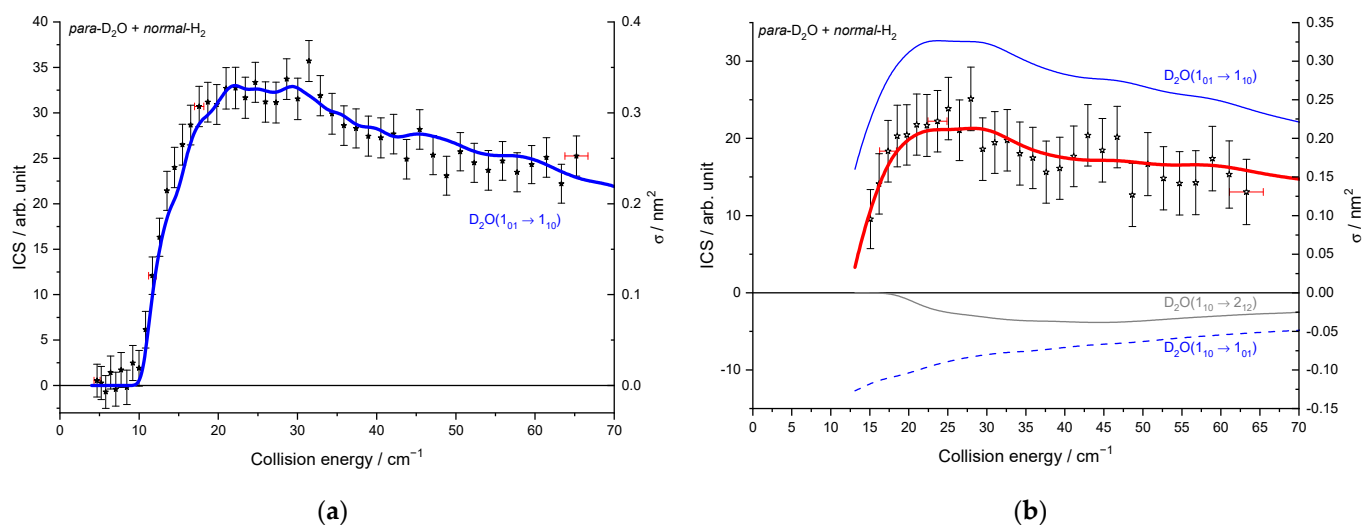


**Figure 9.** Experimental and theoretical cross-sections for the  $D_2O + normal-H_2 \rightarrow D_2O(1_{10}) + normal-H_2$  inelastic collisions. Black squares are experimental ICSs for the 1<sub>10</sub> rotational level, with error bars corresponding to statistical uncertainties at 95% of the confidence interval, in the conditions of (Table 1): (a) D<sub>2</sub>O seeded in Ne and *normal*-H<sub>2</sub> at 10 K (b) D<sub>2</sub>O seeded in He and *normal*-H<sub>2</sub> at 145 K. Negative values for the cross-sections mean that the 1<sub>10</sub> rotational population probed decreases. In red solid line, the total theory contributions are convoluted to experimental resolution, with partial contributions in blue, the 1<sub>01</sub> → 1<sub>10</sub> transition, in blue dotted line, the loss is due to the 1<sub>10</sub> → 1<sub>01</sub> transition, and in gray, the loss is due to the 1<sub>10</sub> → 2<sub>12</sub> transition, assuming the initial rotational population given in Table 2.

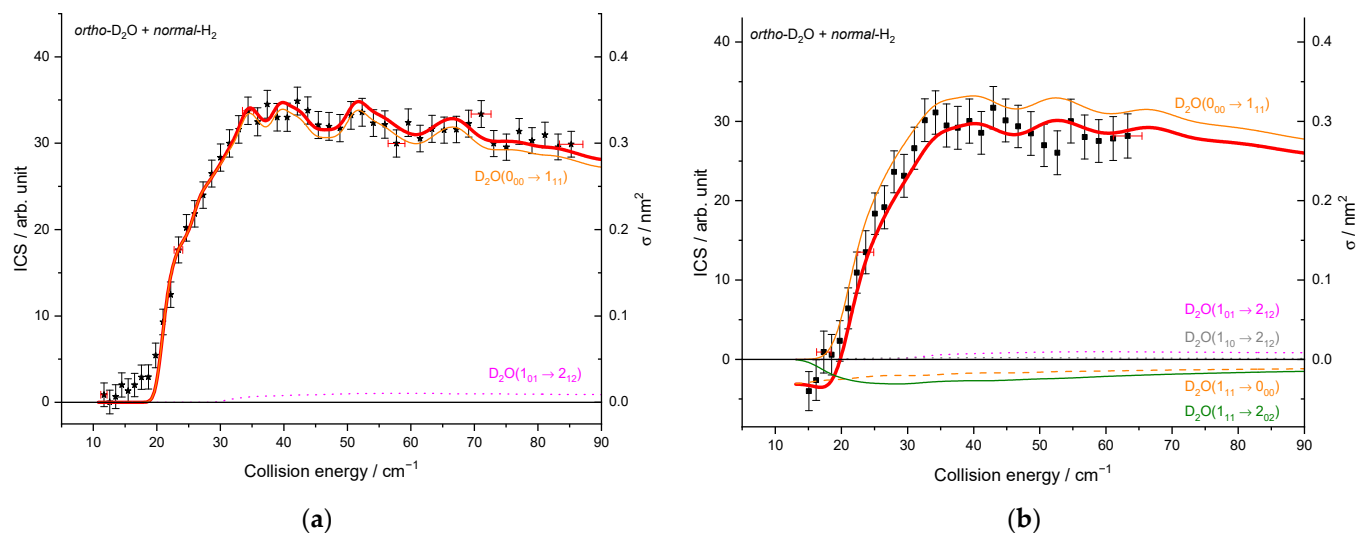


**Figure 10.** Experimental and theoretical cross-sections for the  $D_2O + normal-H_2 \rightarrow D_2O(1_{11}) + normal-H_2$  inelastic collisions. Black squares are experimental ICSs for the 1<sub>11</sub> rotational level, with error bars corresponding to statistical uncertainties at 95% of the confidence interval, in the conditions (Table 1) of: (a) D<sub>2</sub>O seeded in Ne and *normal*-H<sub>2</sub> at 10 K (b) D<sub>2</sub>O seeded in He and *normal*-H<sub>2</sub> at 145 K. Negative values for the cross-sections mean that the 1<sub>11</sub> rotational population probed decreases. In red solid line, the total theory contributions are convoluted to experimental resolution, with partial contributions of the 0<sub>00</sub> → 1<sub>11</sub> transition (in orange solid line), the 1<sub>01</sub> → 2<sub>12</sub> transition (in magenta dotted line), 1<sub>10</sub> → 2<sub>12</sub> transition (in gray), the loss due to the 1<sub>11</sub> → 2<sub>02</sub> transition (in olive), and the loss due to the 1<sub>11</sub> → 2<sub>12</sub> transition (in orange dotted line), assuming the initial rotational population and a partial contribution from the 2<sub>12</sub> state, when probing the 1<sub>11</sub> state, given in Table 2.

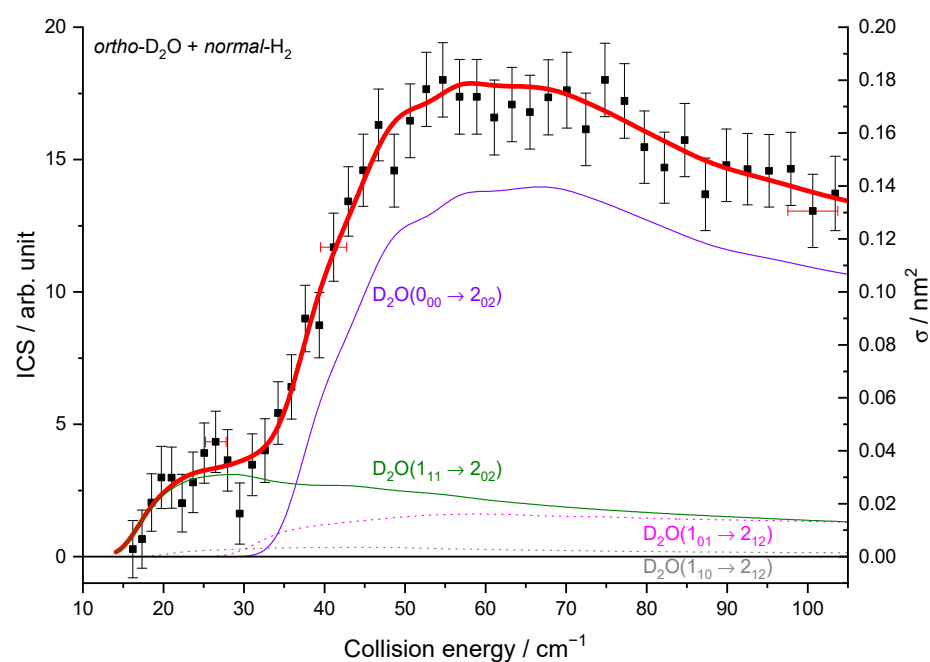


**Figure 11.** Experimental and theoretical cross-sections for the  $D_2O + normal-H_2 \rightarrow D_2O(2_{02}) + normal-H_2$  inelastic collisions in the conditions (Table 1) of  $D_2O$  seeded in He and  $normal-H_2$  at 145 K. Black squares are experimental ICSs for the  $2_{02}$  rotational level, with error bars corresponding to statistical uncertainties at 95% of the confidence interval. In red solid line, the total theory contributions are convoluted to experimental resolution, with partial contributions in violet solid line, the  $0_{00} \rightarrow 2_{02}$  transition, in olive, the  $1_{11} \rightarrow 2_{02}$  transition, in magenta dotted line, the  $1_{01} \rightarrow 2_{12}$  transition, and in gray  $1_{10} \rightarrow 2_{12}$  transition, assuming the initial rotational population and a partial contribution from the  $2_{12}$  state, when probing the  $2_{02}$  state, given in Table 2.

The experiments conducted with  $normal-H_2$  at a given collision energy can only observe the summation of all partial wave contributions weighted by the  $(2J + 1)$  degeneracy factor in the ICSs. The contributions of many overlapping partial waves corresponding to the energetically allowed  $J$ -values tend to average the individual resonance amplitudes, making them interfere and average out. Unfortunately, for the processes with  $para-H_2$ , as explained previously (see Figures 2 and 3), the theoretical calculations predict too small transition probabilities to be experimentally probed at the collision energies close to the thresholds, except for the  $0_{00}$  to  $2_{02}$  rotational excitation of  $D_2O$  [8].

In summary, we were able to observe some resonances in the experimental excitation functions, and the agreement between experiment and theory is excellent in all cases presented herein, for the collision energy range 10–100  $cm^{-1}$ .

While the reduced mass of  $D_2O + H_2$  (1.8313 u) is only slightly different from that of  $H_2O + H_2$  (1.8128 u), the water deuteration can significantly affect inelastic collisional rates: the H/D isotopic substitution results in a difference in the reduced mass, rotational constants, zero-point energies and energies of the quasi-bound states supported by the potential. Additionally, the center of mass is slightly moved. Consequently, the intensities and positions of the resonant peaks will vary. In Figure 12, we have reported the ICSs calculated for the first rotational excitation of  $D_2O$  and  $H_2O$  by collisions with  $normal-H_2$ . To ease the comparison, the rotational energy diagram of  $H_2O$  and  $D_2O$  was added. Note that  $ortho$  and  $para$  systems are inverted due to the nuclear spins (deuteron versus proton).

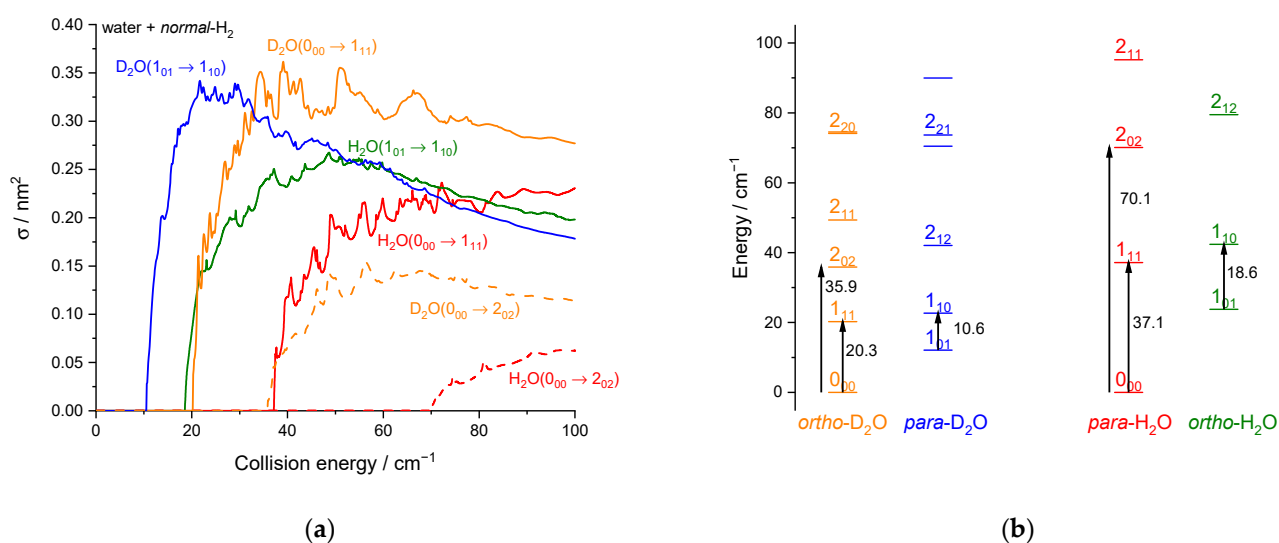


**Figure 12.** D<sub>2</sub>O or H<sub>2</sub>O + *normal*-H<sub>2</sub> rotational inelastic collisions: (a) Theoretical cross-sections of the D<sub>2</sub>O 0<sub>00</sub> → 1<sub>11</sub> transition in orange solid line, the D<sub>2</sub>O 0<sub>00</sub> → 2<sub>02</sub> transition in orange dashed line, the D<sub>2</sub>O 1<sub>01</sub> → 1<sub>10</sub> transition in blue line, the H<sub>2</sub>O 0<sub>00</sub> → 1<sub>11</sub> transition in red solid line, the H<sub>2</sub>O 0<sub>00</sub> → 2<sub>02</sub> transition in red dashed line, and the 1<sub>01</sub> → 1<sub>10</sub> transition in olive line. (b) Rotational energy diagram up to  $j_1 = 2$  with the four transitions shown in panel (a) [7].

We can observe in Figure 12 that the first rotational transitions 0<sub>00</sub> → 1<sub>11</sub> and 1<sub>01</sub> → 1<sub>10</sub> for H<sub>2</sub>O + H<sub>2</sub> and D<sub>2</sub>O + H<sub>2</sub> inelastic collisions. Just after the threshold rise and before the decrease, the excitation ICSs for H<sub>2</sub>O tend to be smaller than those for D<sub>2</sub>O by typically 30% (in qualitative accordance with the energy gap law) while the propensity rules (discussed in the theoretical results section in terms of the dipolar transitions in the C<sub>2v</sub> symmetry) are equivalent for these *b*-type transitions ( $\Delta k_a = \pm 1$ ,  $\Delta k_c = \pm 1$ ). At larger collision energies, the differences between D<sub>2</sub>O and H<sub>2</sub>O tend to be smaller. Thus, for these two dipolar transitions, the differences between D<sub>2</sub>O and H<sub>2</sub>O are not substantial and mainly reflect the kinematics effects (mass and velocities) due to the change in rotational constants and the corresponding different rotational thresholds. For dipole-forbidden transitions, however, much larger differences are observed, as observed in Figure 12a for the transition 0<sub>00</sub> → 2<sub>02</sub> where the cross-section peak for D<sub>2</sub>O exceeds the cross-section plateau for H<sub>2</sub>O by a factor of ~2.5. As explained by Scribano et al. [20], this is due to the non-dipolar interaction terms in the PES, which are more affected by the isotopic substitution than the dipolar terms. As a result, the H/D substitution results both in kinematics and PES effect whose relative importance depends on the type of transition.

## 4. Methods

### 4.1. Theoretical Calculations

As in Bergeat et al. [8], inelastic scattering calculations were performed at the close-coupling level with the MOLSCAT program [32] using a rigid-rotor D<sub>2</sub>O–H<sub>2</sub> potential energy surface (PES) adapted from the full-dimensional H<sub>2</sub>O–H<sub>2</sub> PES of Valiron et al. [22]. The shift of center of mass and change of internal geometries (zero-point vibrational effects) were both taken into account. Full details about the geometrical transformation from H<sub>2</sub>O–H<sub>2</sub> to D<sub>2</sub>O–H<sub>2</sub> can be found in [20], but it should be noted that we found a small error in the implementation of Scribano et al. [20] so that in practice a new rigid-rotor D<sub>2</sub>O–H<sub>2</sub> PES was used in [8] and also herein.

D<sub>2</sub>O is an asymmetric top, and the rotational constants were taken as  $A = 15.41998$ ,  $B = 7.27299$ , and  $C = 4.84529 \text{ cm}^{-1}$ . Centrifugal correction terms were unnecessary for the low-lying levels examined herein. For H<sub>2</sub>, the rotational constant is  $B_0 = 59.322 \text{ cm}^{-1}$ , as in Bergeat et al. [8]. The reduced mass of the D<sub>2</sub>O–H<sub>2</sub> system is 1.8313 u. The coupled



differential scattering equations were solved using the hybrid modified log-derivative Airy propagator for total energies up to  $300\text{ cm}^{-1}$ .

Convergence was carefully checked with respect to the propagator step size. Finally, we used a fine energy grid of  $0.25\text{ cm}^{-1}$ , and the cross-sections were interpolated with a cubic spline in order to convolve them with the experimental collision energy spread ( $\gtrsim 1\text{ cm}^{-1}$ ).

## 4.2. Crossed Molecular Beams

### 4.2.1. Experimental Procedure

We performed our experiments with a crossed-beam apparatus (Figure 2), with a fixed water beam and a rotatable  $\text{H}_2$  beam.

The gas manifold comprises a 0.5 L steel tank of high purity liquid deuterated water into which pure neon or helium is added at 12 bar. The tank is held at  $40\text{ }^\circ\text{C}$ , resulting in a 0.8578 kPa  $\text{D}_2\text{O}$  vapor pressure [33] and 0.07%  $\text{D}_2\text{O}/\text{Ne}$  or  $\text{He}$  gas mixture. This gas mixture is then introduced into the stagnation region of a pulsed Even–Lavie valve (100- $\mu\text{m}$  aperture, 150- $\mu\text{m}$  conical nozzle,  $\sim 10\text{ }\mu\text{s}$  pulse-time, 10 Hz repetition rate) maintained at 320 K to avoid any condensation of water before the supersonic expansion. A turbomolecular pump keeps an average chamber pressure of  $\sim 10^{-6}$  mbar under full pulsed valve operation. The resulting  $\text{D}_2\text{O}$  beam seeded in  $\text{Ne}$  or  $\text{He}$  travels  $\sim 95\text{ mm}$  through the source chamber, separated to the main chamber by a 3-mm inner diameter skimmer. Then, the supersonic molecular beam flies  $\sim 22\text{ cm}$  to the interaction region (with a background pressure  $< 10^{-6}$  mbar), where the second supersonic beam crosses, in perfect synchronization.

*Normal- $\text{H}_2$*  beam pulses were obtained using cryogenically cooled Even–Lavie valve (pulse-time of 7.3 and 5.8  $\mu\text{s}$  for a valve setpoint at 145 or 10 K, respectively) with 12.5–13.5 bar of net hydrogen in the reservoir. The pulsed valve chamber is maintained at  $\sim 10^{-6}$  mbar by a turbomolecular pump and is separated to the main chamber by a 2-mm skimmer 33 mm after the nozzle. This  $\text{H}_2$  source chamber may rotate from  $90^\circ$  to  $13^\circ$  allowing the beam intersection angle to be varied continuously. The distance from the skimmer to the crossing point is  $\sim 6\text{ cm}$  and the time delay between the two pulsed beams was adjusted to ensure a perfect overlap of both beams at the crossing point [24]. To minimize background contributions from any rotationally excited molecules in the water beam or the main chamber, the  $\text{H}_2$  beam is triggered at 5 Hz, with signals averaged in alternating pulse mode and recorded as two intensities: signal and background.

Detection of  $\text{D}_2\text{O}$  rotational levels in its ( $X^1A_1, v = 0$ ) ground vibronic state is achieved in the beam-crossing region by a laser beam perpendicular to the scattering plane.  $\text{D}_2\text{O}$  is detected by REMPI with a 2 + 1 scheme in the UV: two-photon resonant and one-photon ionization at  $\sim 247\text{ nm}$  via the ( $C^1B_1, v' = 0$ ) Rydberg state. The laser system consisted of a dye laser (Coumarin 500) pumped by the third harmonic at 355 nm of an Nd:YAG laser. UV laser pulse energies of 2.5–4.5 mJ per pulse at repetition rate of 10 Hz were generated by doubling the visible laser output in a beta barium borate (BBO) crystal. A small part of the visible dye laser was sent to a wavemeter to control the  $\text{D}_2\text{O}$  rotational state probed, and a photodiode was monitoring the UV laser to ensure that the energy remained constant during scanning. A two-stage time-of-flight mass spectrometer (TOF MS), which has specially cut plates to allow the beams to pass through, is positioned in the beam scattering plane and tilted by  $135^\circ$  to the water supersonic beam. A multichannel plate detector is used for ion detection. The signal is pre-amplified, gated, and integrated using a boxcar over the time-of-flight corresponding to the  $\text{D}_2\text{O}$  mass and recorded to a computer.

To measure velocity distribution, the density temporal profiles of  $\text{D}_2\text{O}$  by REMPI-MS detection at the crossing point and of  $\text{Ne}$  or  $\text{He}$  by a fast ionization gauge (FIG) at  $d = 393.3\text{ mm}$  downstream were recorded and fitted to Gaussian profiles. The detailed procedure was used to extract the density pulse profile, and the velocity distribution was detailed previously [24,34]. Briefly, the Gaussian functions with peak positions  $t_0$  and  $t_1$  and widths  $\gamma_0$  and  $\gamma_1$  yield the peak velocities  $v = d/(t_1 - t_0)$ , and the velocity spreads

from the pulse broadening, taking into account the response time of the fast-ionization gauge. The results are reported in Table 1. To measure the angular divergence of the beams, the TOF-MS was replaced by a second FIG inserted perpendicular to the beam axis. The two density profiles obtained by the two FIGs separated by  $d = 393.3$  mm were measured at different positions of the FIGS perpendicularly to the beam axis: Gaussian fits gave the angular spread reported in Table 1 and the exact beam axis locations. It should be noticed that the beam velocity characterizations obtained by the two FIGs or by the association of the REMPI signal with the far FIG gave the same results.

ICSs were obtained from the REMPI signal intensities of the rotationally excited water molecules,  $D_2O(j_{kake})$ . The intensities, signal, and background were acquired for each individual laser shot and intersection angle. The points associated with too small UV laser intensities were rejected to stay in the linear regime whereby the REMPI intensity only depends on the water density. After subtraction of the background mean for each angle, each signal intensity was normalized by the average value over the whole angle scan, allowing for accumulation of several short-duration scans measured in 2 or 3 days. The conditions for each result set presented are summarized in Table 3. All the plotted vertical error bars on the experimental ICSs represent the combination of statistical fluctuations at a 95% confidence interval of the signal and background data. The plotted error bars on energy are estimated from velocity and crossing angle uncertainties: it represents the uncertainty of the peak collision energy value, not the collision energy spread that is reported in Figure 6b.

**Table 3.** Each experimental ICSs of a specific rotationally excited water molecules,  $D_2O(j_{kake})$  corresponds to a number of laser shots,  $n$ , per angle, scanning the beam intersection angle in the range  $\gamma_{initial}-\gamma_{final}$  with  $-1^\circ$  or  $-0.5^\circ$  decrement.

$D_2O(j_{kake})$	Wavelength	$n$ Laser Shots/Angle	Intersection Angles
$2_{02}$	247.340 nm	2275	$35^\circ-13^\circ (-0.5^\circ)$
$1_{11}$ with $D_2O$ in Ne	247.670 nm	3585	$70^\circ-23^\circ (-1^\circ)$
$1_{11}$ with $D_2O$ in He	247.670 nm	3691	$27^\circ-12.5^\circ (-0.5^\circ)$
$1_{10}$ with $D_2O$ in Ne	247.684 nm	2482	$60^\circ-13^\circ (-1^\circ)$
$1_{10}$ with $D_2O$ in He	247.684 nm	2684	$27^\circ-12.5^\circ (-0.5^\circ)$

The experimental ICSs were obtained from the averaged REMPI signal intensities  $I$ , the relative velocity  $v_r$  of the  $D_2O$  and  $H_2$  beams, and the mean interaction time  $\Delta t$  between the two beam pulses, as  $\sigma = I/(v_r \Delta t)$ . This interaction time, given in Figure 6a, takes full account of the density-to-flux transformation under our working conditions, when modelling pulsed beam densities with spatial and temporal Gaussian distribution functions.

Indeed, the beam crossing region where collisions contribute to the signal is delimited by the waist of the laser beam steered perpendicularly to the beam scattering plane and also by the beam overlap region even far upstream from the crossing point (see Figure 13). In fact, we consider the locus of points  $(x, y)$  for which the product of pulse beam densities  $n_{H_2}(x, y, t) \times n_{D_2O}(x, y, t) = 1/e$ . As at low collision energies (or angles), which correspond to near-threshold collisions, the excited water molecules have almost no recoil energies (or velocities); the scattered  $D_2O$  are therefore travelling in phase with the center-of-mass (cm) velocity vector. For each collision energy, there is only one definite value for the velocity of the recoiling product, the rotationally excited  $D_2O$ , in the center-of-mass frame (Figure 2b). Under all our experimental conditions, the scattered  $D_2O$  product recoils with a velocity in the cm frame, which remains rather low (in the most unfavorable case:  $82 \text{ m s}^{-1}$  for a  $v_{cm} = 809 \text{ m s}^{-1}$ ); its velocity in the laboratory frame thus remains very close to the cm velocity. This induces not only an angular spread and a collision energy spread (Figure 6b) but also a highest value of the mean collision energy at a specific angle relative to the beam axes,  $\gamma$  due to a shift of the mean value of crossing angle [34]. In the  $\Delta t$  calculations, the angular distribution of scattered species was also taken into account. However, in our previous study on inelastic collisions between  $D_2O$  and *para*- $H_2$  [8], the differential cross-sections were also calculated, and it was shown that the collisions were

backward, forward, backward-forward, or isotropic: the dynamics were varying with the collision energy. As the angular distribution (forward or isotropic) was found to have an almost negligible impact on the time-interaction values, we have simplified the analysis, considering an isotropic distribution of the products at all collision energies for all the rotationally excited D<sub>2</sub>O products.

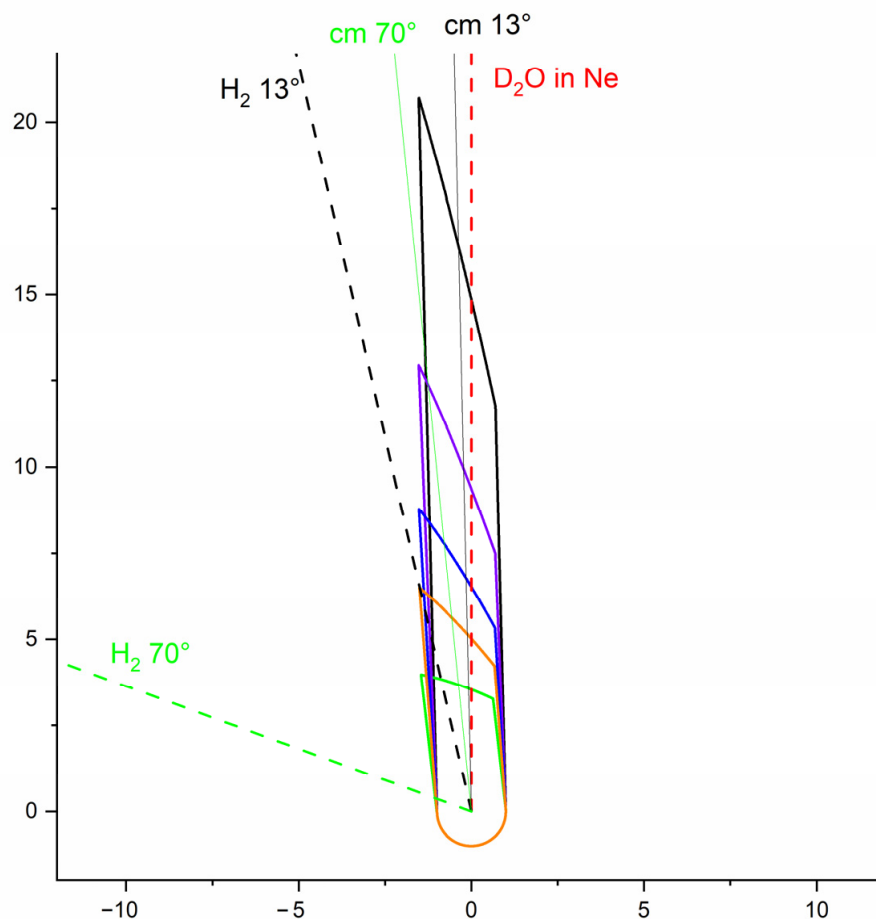


**Figure 13.** The interaction volumes taken into account in the density-to-flux transformation for different crossing angles relatively to the water beam: in black 13°, in violet 21°, in blue 31°, in orange 42°, and in green 70°. The red dashed line is the D<sub>2</sub>O:Ne beam axis. The black and green dashed lines are the H<sub>2</sub> beam axis, and the black and green solid lines are the center-of-mass velocity vectors, for a crossing angle of 13° and 70°, respectively.

#### 4.2.2. Data Treatment for Comparisons

The total inelastic collision cross-section  $\sigma_{i \rightarrow f}$  is related to the overall probability that an inelastic transition will take place from the rotational state  $|i\rangle$  of D<sub>2</sub>O to the state  $|f\rangle$  by collisions with *normal*-H<sub>2</sub>. The bimolecular rate will induce a transition  $|i\rangle \rightarrow |f\rangle$  in D<sub>2</sub>O is:

$$\frac{dn_f}{dt} = n_{H_2} n_i k_{i \rightarrow f}(v_r) = n_{H_2} n_{D_2O} p(i) v_r \sigma_{i \rightarrow f}(v_r) \quad (3)$$

where  $k_{i \rightarrow f}(v_r)$  is the rate constant at relative velocity  $v_r$ ,  $n_{H_2}$  the number density of the H<sub>2</sub> collision partner,  $n_{D_2O}$  the D<sub>2</sub>O number density, and  $p(i)$  the population of D<sub>2</sub>O in the rotational state  $|i\rangle$ .

The rate law for the inelastic collisions between D<sub>2</sub>O and H<sub>2</sub> of a particular probed rotational level  $|f\rangle$  density ( $n_f$ ) is thus:

$$\begin{aligned} \frac{dn_f}{dt} &= n_{H_2} n_{D_2O} \sum_{i \neq f} p(i) k_{i \rightarrow f}(v_r) - n_{H_2} n_{D_2O} p(f) \sum_{l \neq f} k_{f \rightarrow l}(v_r) \\ &= n_{H_2} n_{D_2O} v_r \left( \sum_{i \neq f} p(i) \sigma_{i \rightarrow f}(v_r) - p(f) \sum_{l \neq f} \sigma_{f \rightarrow l}(v_r) \right) \end{aligned} \quad (4)$$

where the first term corresponds to filling up the state  $|f\rangle$ , and the second term is related to the loss of population out of this initial level  $f$  level.  $\sigma_{i \rightarrow f}$  are the cross-sections from all the populated levels  $|i\rangle$  to the  $|f\rangle$  state when the relative velocity between D<sub>2</sub>O, and H<sub>2</sub> is equal to  $v_r$ ,  $p(i)$  is the population ratio in the state  $|i\rangle$ , and  $\sigma_{f \rightarrow l}$  the cross-sections of the  $|f\rangle \rightarrow |l\rangle$  transitions if the probed level  $|f\rangle$  is initially populated ( $p(f)$ ). The REMPI intensity is proportional to the D<sub>2</sub>O density of the  $f$  rotational level probed,  $n_f$ . However, as we do not know the exact densities of D<sub>2</sub>O and H<sub>2</sub> in our beams, the experimental ICSs are given in arbitrary units. To compare the experimental ICSs with the theoretical ones, we have thus added or subtracted the calculated cross-sections weighted by the appropriate initial rotational population (see Table 2).

Moreover, at the wavelength of 247.34 or 247.67 nm chosen to probe the  $2_{02}$  or  $1_{11}$  rotational level of D<sub>2</sub>O, there is a small contribution from the  $2_{12}$  level. Thus, the ICSs of the  $1_{01} \rightarrow 2_{12}$  and  $1_{10} \rightarrow 2_{12}$  were considered with weights taking into account the relative rotational populations and the relative strength of the REMPI transitions from the  $2_{02}$  or  $1_{11}$  and  $2_{12}$  levels (see Table 2).

Each theoretical cross-section is calculated for one collision energy or relative velocity of D<sub>2</sub>O and H<sub>2</sub> (Equation (1)), but the experimental values are resulting from the integration over collision energy spread. To compare theory and experiment, the calculated excitation functions were convoluted with our experimental energy spread (Figure 2), and the experimental data were multiplied by a unique scaling value.

**Author Contributions:** Conceptualization, A.B. and C.N.; laser, S.B.M. and A.B.; experimental investigation, A.B. and C.M. (Master internship); calculations, L.W. and A.F.; funding acquisition, A.B. and A.F.; writing, A.B., A.F. and L.W. All authors have read and agreed to the published version of the manuscript.

**Funding:** This research was supported by the Programme National « Physique et Chimie du Milieu Interstellaire » (PCMI) of the CNRS/INSU with INC/INP co-funded by CEA and CNES. The experimental research was also funded by Agence Nationale de la Recherche, grant number ANR-20-CE31-0011.

**Institutional Review Board Statement:** Not applicable.

**Informed Consent Statement:** Not applicable.

**Data Availability Statement:** Data is contained within the article and may be obtained in another format on request from the authors.

**Conflicts of Interest:** The authors declare no conflict of interest. The funders had no role in the design of the study; in the collection, analyses, or interpretation of data; in the writing of the manuscript; or in the decision to publish the results.

**Sample Availability:** Samples of the compounds are available from the authors.

## References

1. Cheung, A.C.; Thornton, D.D.; Rank, D.M.; Welch, W.J.; Townes, C.H. Detection of Water in Interstellar Regions by its Microwave Radiation. *Nature* **1969**, *221*, 626–628. [CrossRef]
2. Van Dishoeck, E.F.; Kristensen, L.E.; Mottram, J.C.; Benz, A.O.; Bergin, E.A.; Caselli, P.; Herpin, F.; Hogerheijde, M.R.; Johnstone, D.; Liseau, R.; et al. Water in star-forming regions: Physics and chemistry from clouds to disks as probed by Herschel spectroscopy. *A&A* **2021**, *648*, A24–A57. [CrossRef]
3. Jensen, S.S.; Jorgensen, J.K.; Furuya, K.; Haugbolle, T.; Aikawa, Y. Modeling chemistry during star formation: Water deuteration in dynamic star-forming regions. *A&A* **2021**, *649*, A21–A66. [CrossRef]

4. Butner, H.M.; Charnley, S.B.; Ceccarelli, C.; Rodgers, S.D.; Pardo, J.R.; Parise, B.; Cernicharo, J.; Davis, G.R. Discovery of interstellar heavy water. *Astrophys. J.* **2007**, *659*, L137–L140. [[CrossRef](#)]
5. Vastel, C.; Ceccarelli, C.; Caux, E.; Coutens, A.; Cernicharo, J.; Bottinelli, S.; Demyk, K.; Faure, A.; Wiesenfeld, L.; Scribano, Y.; et al. Ortho-to-para ratio of interstellar heavy water. *A&A* **2010**, *521*, L31–L35. [[CrossRef](#)]
6. Levine, R.D.; Bernstein, R.B. *Molecular Reaction Dynamics and Chemical Reactivity*; Oxford University Press: New York, NY, USA, 1987.
7. Gordon, I.E.; Rothman, L.S.; Hargreaves, R.J.; Hashemi, R.; Karlovets, E.V.; Skinner, F.M.; Conway, E.K.; Hill, C.; Kochanov, R.V.; Tan, Y.; et al. The HITRAN2020 molecular spectroscopic database. *J. Quant. Spectrosc. Radiat. Transf.* **2022**, *277*, 107949. [[CrossRef](#)]
8. Bergeat, A.; Morales, S.B.; Naulin, C.; Wiesenfeld, L.; Faure, A. Probing Low-Energy Resonances in Water-Hydrogen Inelastic Collisions. *Phys. Rev. Lett.* **2020**, *125*, 143402. [[CrossRef](#)]
9. Zoltowski, M.; Lique, F.; Karska, A.; Zuchowski, P.S. Rotational excitation of highly excited H<sub>2</sub>O by H<sub>2</sub>. *MNRAS* **2021**, *502*, 5356–5361. [[CrossRef](#)]
10. Bickes, R.W., Jr.; Duquette, G.; van den Meijdenberg, C.J.N.; Rulis, A.M.; Scoles, G.; Smith, K.M. Molecular beam scattering experiments with polar molecules: Measurement of differential collision cross sections for H<sub>2</sub>O+H<sub>2</sub>, He, Ne, Ar, H<sub>2</sub>O and NH<sub>3</sub>+H<sub>2</sub>, He, NH<sub>3</sub>. *J. Phys. B Atom. Mol. Phys.* **1975**, *8*, 3034–3043. [[CrossRef](#)]
11. Weida, M.J.; Nesbitt, D.J. High-resolution diode laser study of H<sub>2</sub>–H<sub>2</sub>O van der Waals complexes: H<sub>2</sub>O as proton acceptor and the role of large amplitude motion. *J. Chem. Phys.* **1999**, *110*, 156–167. [[CrossRef](#)]
12. Ziemkiewicz, M.P.; Pluetzer, C.; Nesbitt, D.J.; Scribano, Y.; Faure, A.; van der Avoird, A. Overtone vibrational spectroscopy in H<sub>2</sub>-H<sub>2</sub>O complexes: A combined high level theoretical ab initio, dynamical and experimental study. *J. Chem. Phys.* **2012**, *137*, 084301. [[CrossRef](#)] [[PubMed](#)]
13. Forney, D.; Jacox, M.E.; Thompson, W.E. Infrared absorptions of the H<sub>2</sub>O-H<sub>2</sub> complex trapped in solid neon. *J. Chem. Phys.* **2004**, *121*, 5977–5984. [[CrossRef](#)] [[PubMed](#)]
14. Dutta, J.M.; Jones, C.R.; Goyette, T.M.; de Lucia, F.C. The Hydrogen and Helium Pressure Broadening at Planetary Temperatures of the 183 and 380 GHz Transitions of Water Vapor. *Icarus* **1993**, *102*, 232–239. [[CrossRef](#)]
15. Drouin, B.; Wiesenfeld, L. Low-temperature water–hydrogen-molecule collisions probed by pressure broadening and line shift. *Phys. Rev. A* **2012**, *86*, 022705. [[CrossRef](#)]
16. Yang, C.-H.; Sarma, G.; Parker, D.H.; ter Meulen, J.J.; Wiesenfeld, L. State-to-state differential and relative integral cross sections for rotationally inelastic scattering of H<sub>2</sub>O by hydrogen. *J. Chem. Phys.* **2011**, *134*, 204308. [[CrossRef](#)]
17. Bergeat, A.; Faure, A.; Morales, S.B.; Moudens, A.; Naulin, C. Low-Energy Water–Hydrogen Inelastic Collisions. *J. Phys. Chem. A* **2020**, *124*, 259–264. [[CrossRef](#)]
18. Belpassi, L.; Reça, M.L.; Tarantelli, F.; Roncaratti, L.F.; Pirani, F.; Cappelletti, D.; Faure, A.; Scribano, Y. Charge-Transfer Energy in the Water-Hydrogen Molecular Aggregate Revealed by Molecular-Beam Scattering Experiments, Charge Displacement Analysis, and ab Initio Calculations. *J. Am. Chem. Soc.* **2010**, *132*, 13046–13058. [[CrossRef](#)]
19. van der Avoird, A.; Scribano, Y.; Faure, A.; Weida, M.J.; Fair, J.R.; Nesbitt, D.J. Intermolecular potential and rovibrational states of the H<sub>2</sub>O–D<sub>2</sub> complex. *Chem. Phys.* **2012**, *399*, 28–38. [[CrossRef](#)]
20. Scribano, Y.; Faure, A.; Wiesenfeld, L. Communication: Rotational excitation of interstellar heavy water by hydrogen molecules. *J. Chem. Phys.* **2010**, *133*, 231105. [[CrossRef](#)]
21. Faure, A.; Wiesenfeld, L.; Scribano, Y.; Ceccarelli, C. Rotational excitation of mono- and doubly-deuterated water by hydrogen molecules. *MNRAS* **2012**, *420*, 699–704. [[CrossRef](#)]
22. Valiron, P.; Wernli, M.; Faure, A.; Wiesenfeld, L.; Rist, C.; Kedzuch, S.; Noga, J. R12-calibrated H<sub>2</sub>O-H<sub>2</sub> interaction: Full dimensional and vibrationally averaged potential energy surfaces. *J. Chem. Phys.* **2008**, *129*, 134306-14. [[CrossRef](#)] [[PubMed](#)]
23. Sarma, G.; Yang, C.-H.; Saha, A.K.; Parker, D.H.; Wiesenfeld, L. Rotational excitation of HDO and D<sub>2</sub>O by H<sub>2</sub>: Experimental and theoretical differential cross-sections. *J. Chem. Phys.* **2013**, *138*, 024314. [[CrossRef](#)] [[PubMed](#)]
24. Bergeat, A.; Morales, S.B.; Naulin, C.; Klos, J.; Lique, F. Quantum Behavior of Spin-Orbit Inelastic Scattering of C-Atoms by D<sub>2</sub> at Low Energy. *Front. Chem.* **2019**, *7*, 164. [[CrossRef](#)] [[PubMed](#)]
25. Yang, C.-H.; Sarma, G.; ter Meulen, J.J.; Parker, D.H.; Western, C.M. REMPI spectroscopy and predissociation of the C<sup>1</sup>B<sub>1</sub>(v = 0) rotational levels of H<sub>2</sub>O, HOD and D<sub>2</sub>O. *Phys. Chem. Chem. Phys.* **2010**, *12*, 13983–13991. [[CrossRef](#)]
26. Western, C.M. PGOPHER, A Program for Simulating Rotational, Vibrational and Electronic Spectra. *J. Quant. Spectrosc. Radiat. Trans.* **2017**, *186*, 221–242. [[CrossRef](#)]
27. Ziemkiewicz, M.P.; Pluetzer, C.; Wojcik, M.; Loreau, J.; van der Avoird, A.; Nesbitt, D.J. Near infrared overtone (ν<sub>OH</sub> = 2 ← 0) spectroscopy of Ne-H<sub>2</sub>O clusters. *J. Chem. Phys.* **2017**, *146*, 104204. [[CrossRef](#)]
28. Hou, D.; Ma, Y.-T.; Zhang, X.-L.; Li, H. A full-dimension intra- and inter-molecular ab initio potential energy surface and predicted infrared spectra for H<sub>2</sub>O-He. *J. Mol. Spectrosc.* **2016**, *330*, 217–227. [[CrossRef](#)]
29. Pratt, S.T.; Dehmer, P.M.; Dehmer, J.L. Photoionization of excited molecular states. H<sub>2</sub> C<sup>1</sup>Π<sub>u</sub>. *Chem. Phys. Lett.* **1984**, *105*, 28. [[CrossRef](#)]
30. Ma, Q.; van der Avoird, A.; Loreau, J.; Alexander, M.H.; van de Meerakker, S.Y.T.; Dagdigan, P.J. Resonances in rotationally inelastic scattering of NH<sub>3</sub> and ND<sub>3</sub> with H<sub>2</sub>. *J. Chem. Phys.* **2015**, *143*, 044312. [[CrossRef](#)]
31. van der Avoird, A.; Nesbitt, D.J. Rovibrational states of the H<sub>2</sub>O–H<sub>2</sub> complex: An ab initio calculation. *J. Chem. Phys.* **2011**, *134*, 044314. [[CrossRef](#)]

32. Hutson, J.M.; Green, S. *MOLSCAT: MOLEcular SCATtering*, Version 14; Astrophysics Source Code Library: Houghton, MI, USA, 2012; Available online: <https://ui.adsabs.harvard.edu/abs/2012ascl.soft06004H/abstract> (accessed on 20 September 2022).
33. Harvey, A.H.; Lemmon, E.W. Correlation for the Vapor Pressure of Heavy Water from the Triple Point to the Critical Point. *J. Phys. Chem. Ref. Data* **2002**, *31*, 173–181. [[CrossRef](#)]
34. Naulin, C.; Bergeat, A. Low-energy Scattering in Crossed Molecular Beams. In *Book Cold Chemistry: Molecular Scattering and Reactivity Near Absolute Zero*; Osterwalder, A., Dulieu, O., Eds.; The Royal Society of Chemistry: London, UK, 2018; pp. 92–149.